https://doi.org/10.5194/egusphere-2026-1440
Preprint. Discussion started: 18 March 2026

Estimation of sea ice air-bubble and brine pocket distribution for scattering and emission model parametrization

Rasmus T. Tonboe[1], Vishnu Nandan[2,3], Marcus Huntemann[4], Julienne Stroeve[5], Randall Scharien[6], John Yackel[3], Lars Kaleschke[7], Hoyeon Shi[8], and Tânia Casal[9]

[1]National Space Institute, Technical University of Denmark, Kongens Lyngby, Denmark
[2]University of Tromsø, Tromsø, Norway
[3]Department of Geography, University of Calgary, Calgary, Alberta, Canada
[4]University of Bremen, Bremen, Germany
[5]University of Manitoba, Winnipeg, Manitoba, Canada
[6]Department of Geography, University of Victoria, Victoria, British Columbia, Canada
[7]Alfred Wegener Institute, Bremerhaven, Germany
[8]NCKF, Danish Meteorological Institute, Copenhagen, Denmark
[9]ESTEC, European Space Agency, Noordwijk, the Netherlands

Correspondence: R. T. Tonboe (rtt@space.dtu.dk)

Abstract. Scattering and absorption from air bubbles, voids, and brine pockets significantly affect radar and microwave radiometer measurements of sea ice and light propagation through sea ice. However, there are only a limited number of *in situ* measurements of the size of natural sea ice inclusion and its distribution. Here, we used a high-resolution data set of 90-mm wide and 1-mm thin ice slices of various types of Arctic sea ice to estimate the autocorrelation length and density of the inclusions. The data set was collected during the MOSAiC International Arctic Drift Expedition 2019-20 during the winter months of January and February 2020. Thin ice slices from new ice, first-year ice, level second-year ice, second-year hummocks, and a refrozen melt pond were collected and analyzed. The 50-percentile autocorrelation lengths derived (L^{obs}), a measure of the size and distribution of inclusions, for new ice and brine ice brine pockets of the first-year have mean values between 0.11 and 0.30 mm and a vertical anisotropy ratio (L_z) and horizontal (L_x) of 1.7-3.0 with respect to the ice surface. The exponential model was fitted to the observed autocorrelation function with a delay between 0-2L^{obs}. The exponential correlation lengths derived (L^{exp}) correspond to the 50 percentile L^{obs} for the ordinary (horizontal) image samples (L_x^{exp}) and the transposed (vertical) images (L_z^{exp}). For new and first-year ice with varying salinity and brine pocket image density, the autocorrelation length is a very robust measure of the size and distribution of brine pockets. For new ice, we find a L_x^{obs} or L_x^{exp} of 0.18 mm and with a L_z/L_x anisotropy of 2 and for first-year ice, we find a L_{obs} or L_{exp} of 0.16 mm with a L_z/L_x anisotropy of 3. The samples from the hummock and the refrozen melt pond had 50 percentile L_x^{obs} and L_z^{obs} air bubble autocorrelation lengths varying in the range $[0.22, 0.73]$ mm and $[0.22, 0.74]$ mm and $[0.17, 0.56]$ mm and $[0.17, 0.79]$ mm, respectively. The very consistent L^{obs} for new and first-year ice can be used to constrain sea ice microwave emission and scattering models.

https://doi.org/10.5194/egusphere-2026-1440
Preprint. Discussion started: 18 March 2026

1 Introduction

During the formation and growth of sea ice, liquid brine is trapped between the ice crystals in brine pockets (Nakawo and Sinha (1984), Weeks and Ackley (1986)). The dynamics, e.g. wave action, of the freezing ocean waters can affect the orientation of frazil crystals in the upper layers of the ice until a continuous sea ice cover is established and the vertically oriented crystals start to dominate. The salinity in first-year ice (FYI) is a function of the salinity of the water and the ice growth rate and subsequent brine migration processes through gravity drainage and brine expulsion (Nakawo and Sinha (1981), Nakawo and Sinha (1984), Shokr and Sinha (2023)). FYI that survives the summer melt and becomes second-year ice (SYI) at the end of the summer is drained of its brine from the upper part of the ice and replaced by voids and air bubbles (e.g., Weeks and Ackley (1986)). The winter multiyear ice (MYI) surface includes hummocks, which are partially melted and refrozen deformation features (ridges), recrystallized snow, snow-ice, refrozen melt ponds and leads in between the floes with their own characteristic microstructure (Shokr and Sinha (2016)). Several studies have characterized the microstructure in FYI to investigate brine migration processes (e.g. Pringle et al. (2009); O'Sadnick et al. (2016); Lieblappen et al. (2018); Oggier and Eicken (2022)). However, only a few studies have been conducted to characterize the statistical description of the sea ice microstructure for input to microwave emission and scattering models (e.g. Perovich and Gow (1991)).

Since the dielectric permittivity of liquid brine is much higher than that of ice at microwave frequencies, and the permittivity of air bubbles is much lower, the density of brine pockets and air bubbles, size, shape and orientation affect the microwave permittivity, loss, and scattering in sea ice (see, e.g., Perovich and Gow (1991); Shokr (1998b); Ulaby and Long (2014); Shokr and Sinha (2016)). The scattering from brine pockets and air void inclusions and the sea ice permittivity affect the radar and microwave radiometer measurements of sea ice. The microstructure of sea ice is therefore important when understanding measured radar and microwave radiometer backscatter and brightness temperatures (T_B), quantifying uncertainties in sea ice concentration estimates using the T_Bs, and setting up microwave emission and scattering models for sea ice for various applications (e.g., Vallese and Kong (1981); Nghiem et al. (1995a); Tonboe et al. (2022); Tonboe (2023)).

The microwave scattering from snow, and in some cases sea ice, is a dense medium, i.e. the scattering from individual snow grains, brine pockets, and voids is not independent of neighboring scatters when the spacing between them is less than the electromagnetic wavelength and the far-field approximation is no longer valid (Mätzler (1987, 1998)). Therefore, classical scattering models for single scatters, such as the Rayleigh approximation model and the Lorenz-Mie scattering model, cannot be applied directly for sea ice. Instead, dense media theory treats densely packed scatters in sea ice (Tsang and Ishimaru (1987)). In addition, the Born approximation for scattering in media with weak dielectric contrasts was improved to describe the strong dielectric contrasts in snow and to accommodate different inclusion (snow grain) shapes (Mätzler (1998)). The Born and improved Born approximations have also been applied for scattering in sea ice (e.g., Nghiem et al. (1995a); Tonboe et al. (2006, 2022)). An exponential autocorrelation function (ACF) with its associated mean, variance, and autocorrelation length (L) describes permittivity fluctuations in ice (Vallese and Kong (1981)). More specifically, the input to the improved Born approximation for scattering is the electromagnetic wave number, the volume density of the scatters, L, the permittivity of the host and the scatters, and the effective permittivity of the mixture (Mätzler (1998))). The input to the mixing formulae used to calculate the permittivity of sea ice is the shape of the inclusions, the volume density of the inclusions, and the permittivity of the host material and inclusions (e.g. Shokr (1998a); Ulaby and Long (2014)). Vallese and Kong (1981) found that L corresponds to the actual size of air bubbles in the ice. However, there are few direct measurements of the inclusion density (I_{ID}) and L in naturally grown sea ice in the literature. Here we adapt the same convention for naming autocorrelation lengths as in Vallese and Kong (1981) and in Nghiem et al. (1995b): L_x and L_y are the perpendicular horizontal autocorrelation lengths and L_z is the vertical autocorrelation length. Vallese and Kong (1981) analyzed L for a sample at 30-40 cm depth in lake ice and found the autocorrelation length in the horizontal direction $L_x = 0.15$ mm and in the vertical direction $L_z = 3$ mm (these numbers have been divided by two due to a different definition of L in Vallese and Kong (1981)). For sea ice Nghiem et al. (1995b) found in a sensitivity analysis that multiyear ice $L_x = 2$ mm and $L_z = 3$ mm and for first-year ice (1 m thick) there was a horizontal and a vertical anisotropy where $L_x = 1.2$ mm and $L_y = 2.2$mm and $L_z = 3.6$ mm. For lead ice (new ice, 3.5 cm thick) the horizontal anisotropy was even greater $L_x = 0.4$ mm, $L_y = 2.8$ mm, and $L_z = 3$ mm.

In order to be able to characterize and parameterize both permittivity and scattering in sea ice, we will analyze a high resolution sea ice data set (see Section 2) collected during the MOSAiC expedition to derive the volume density of scatterers and L in different types of sea ice during mid-winter. The focus is on the upper 0.4 m of the ice, which dominates the variation of 5-100 GHz microwave signatures.

The MOSAiC expedition and an overview of the expedition scientific program are described in Nicolaus et al. (2022). For an overview map, see Figures 1 and 2 in Nicolaus et al. (2022). The data set is limited to the period between 16 January and 22 February 2020 and contains only samples from the ice types found near the ship (new ice, first-year ice (FYI), level second-year ice (SYI), SYI hummock and refrozen melt pond). However, the samples are analyzed at very high vertical resolution and, therefore, this data set provides constraints on parameterization of emission and scattering models and supports advances in our understanding of sea ice microwave remote sensing.

2 Data

The data set consists of photographs of thin sections of sea ice (dimensions approximately $9 \times 9 \times 0.1 - 0.2$ cm) and the salinity of the melted samples collected from Arctic sea ice during Leg 2 of the MOSAiC expedition between 16 January and 22 February 2020. Table 1 shows a list of the dates when the samples were extracted and Figure 1 illustrates the sampling locations. Several different types of sea ice were collected in the area around the ship, R/V Polarstern: new ice, FYI, level SYI, SYI hummock, and refrozen melt pond. All samples were processed in the cold lab onboard R/V Polarstern during the evening during the day when the samples were extracted or the next day to minimize recrystallization and brine migration. The cold lab was a temperature-controlled laboratory at -15^oC and the samples were photographed at that temperature. A total of 25 sea ice cores were analyzed. Since the application is microwave remote sensing, the focus is on the upper approximately 45 cm of the ice corresponding to the penetration and emission layer depth in new ice and FYI for frequencies between approximately 5 and 100 GHz (Tonboe et al. (2006)). It is also the section of the ice where the highest gradients in salinity and density are normally found (e.g. Nakawo and Sinha (1981), Weeks and Ackley (1986)).

https://doi.org/10.5194/egusphere-2026-1440
Preprint. Discussion started: 18 March 2026

Table 1 lists the dates with samples.

2.1 Thin section procedure

All sea ice samples were extracted using the following procedure (and Figure 2):

1. A sea ice core of about 45 cm length was extracted with a 9 cm diameter Kovacs ice corer, bagged, and brought to the cold laboratory.
2. The core was divided into approximately 10 cm sections with a band saw weighted and the dimensions were measured with a ruler for density estimation.
3. The 10 cm core sections were cut horizontally, in a slice (circle), or vertically split into half (square).
4. A glass plate was glued to the sample using distilled water, the sample was reduced to a thickness of approximately 2 cm with a band saw and the free side was smoothed with a diatom slicer.
5. Another glass plate was glued to the smoothed side with distilled water, and then the two glass plates were separated in the middle with the band saw.
6. The sample with the smooth back side glued to the glass was smoothed and thinned with the diatome slicer to a thickness of 1 to 2 mm. Some of the samples with high salinity or porosity were brittle and could not be thinned as much as those samples with lower salinity or porosity.
7. The thinned sample on the glass plate was photographed using a 5M pixel camera on a photopedestal illuminated with a diffuse light source from below.
8. The remaining pieces of the core not used for the photo sample were bagged and melted to measure the salinity.
9. Separate cores were extracted in some cases in the vicinity for salinity analysis.

We have used a methodology for analyzing the data that has also been used to analyze snow data (Wiesmann et al. (1998)).

2.2 Pre-processing of the images

The diameter of the cores is 9 cm, except the level SYI sample collected on 16 January 2020, which had a diameter of 7 cm. Each sample photograph was displayed, and the pixel spacing in the image was estimated manually by locating the 9 cm wide sample edges in the photograph. The corners of a quadrant were then manually selected in the sample photograph. For the vertical samples of the cores, the quadrant side length was close to 9 cm (the actual width of the sample) and the horizontal samples of the cores, the quadrant side length was approximately 6.4 cm. However, some image samples are shorter because of water leakage and cracking of the ice along the edges and resulting unsuccessful classification. These parts of the image have been discarded. Figure 3 shows an example of a FYI sample photograph from Dark Site at 0.1-0.2 m depth, sampled on

https://doi.org/10.5194/egusphere-2026-1440
Preprint. Discussion started: 18 March 2026

5 February 2020. This photograph has shading along the bottom and sides as a result of the "ice-glue" fixing the ice sample to the glass plate. The visible light refractive index of air is 1, ice ~ 1.31, and water ~ 1.33, and because there is a clear contrast in the image sample between what is seen as background ice and what are brine pockets and channels, we believe that the brine has drained during the processing of the FYI samples and that the dark patches/ inclusions in the sample are now filled with air. The inclusions in the melt pond, level second year ice and hummocks are filled with air.

Figure 4 shows the binary classification of the photograph in Figure 3 used for the analysis. The photographs are converted to grayscale with 256 pixel values. Due to uneven illumination of the sample, there is a brightness trend across the sample. To compensate for that, we are using an adaptive threshold classification method using the Python implementation of the CV2 library) with a 501 x 501 pixel window ($\sim$ 0.015 x 0.015 m) and a threshold in the window mean minus 30. This threshold has been experimentally found. The same procedure is used for all ice type samples.

3 Method

All images were processed individually because sections of the images with shades of the "ice-glue" used to fix the slices to the glass plate and other obvious artifacts, such as large cracks, were discarded. No filtering was applied. After manual image cropping, adaptive threshold classification was applied, and then the image analysis included estimation of the inclusion density, exponential fit of the model to the autocorrelation function, and autocorrelation length. The images were analyzed in two directions; for the cores that were cut in the vertical direction, we first analyze the image line-by-line parallel to the ice surface, we call this the *ordinary* direction for estimating L_x, and then we transpose the image matrix to repeat the analysis line-by-line, this time perpendicular to the ice surface; we call this the *transposed* direction for estimating L_z. These directions are visualized in Figure 2 for a better understanding. The estimated ACF of the image in Figure 4 is shown in Figure 5 and a histogram of L_x and L_z line by line is shown in Figure 6.

All estimated autocorrelation functions (ordinary and transposed) are shown in Figure 7. The length of the shift varies as a function of the resolution of the image pixel (3×10^{-5} m) and the length of the line ($\sim 0.08 - 0.09$ m).

The autocorrelation length, L, is the shift in meters for which the value of the autocorrelation function, ACF, has dropped from 1 at 0 m shift to e^{-1} (0.37) at L shift (see Figure 5), i.e.,

$$ACF\,(L) = e^{-1} \tag{1}$$

e^{-1}, is the level of correlation where the line and the shifted line are independent. To evaluate coherence with autocorrelation, a number of independent samples are needed in the sample line to estimate the "true" autocorrelation length, L_0. Estimating the number of independent samples is not trivial. However, when the sample line is longer than $200L_0$ and when there are no underlying trends, then the length of the sample line is sufficient. If the sample line is shorter, the estimated correlation length is underestimated and is a function of the length of the section. Estimates with larger systematic uncertainties can still be made for short sections up to a length of $50L_0$ (Dierking (1999)). Due to the diameter of the corer, the length of the sections is less than or equal to 0.09 m, and then estimates of the correlation length can be made with low uncertainty up to 0.45 mm ($200L_0$)

https://doi.org/10.5194/egusphere-2026-1440
Preprint. Discussion started: 18 March 2026

and with greater systematic uncertainty up to 1.8 mm ($50L_0$). This includes on average all the samples that we have analyzed, but we have anyway estimated the autocorrelation lengths of individual lines up to ∼2.1 mm, although these lines do not meet the criteria.

The autocorrelation length, L^{obs}, is estimated for each line in the ordinary image sample (L_x^{obs}) and the transposed sample (L_z^{obs}) (see Figures 5 and 7), which gives two distributions of the estimated L^{obs} for each image sample as shown in Figure 6. These distributions are not Gaussian and, in addition to the mean value, we have also computed the 2.5, 50, and 97.5 percentiles of the distribution.

The one-parameter exponential model in Equation 2 has been fitted to the autocorrelation function using least squares and within the shift range [0-2L^{obs}]. We use Python *scipy.optimize* to fit the exponential function to the ACF. The exponential function, ACF_{exp}:

$$ACF_{exp} = \exp[-\frac{x}{L^{exp}}], \tag{2}$$

where L^{exp} is the autocorrelation length of the fitted exponential model. Because there were too many cases where Equation 2 could not be fitted to the autocorrelation function of individual lines, the exponential model has been fitted to the average autocorrelation function of all lines in the image sample.

The Gaussian model was also tested, but in all cases the exponential model made a better fit with the estimated autocorrelation function, and therefore we only use the exponential model here, as in Vallese and Kong (1981) and Nghiem et al. (1995b). The resolution of the pixels is approximately 3×10^{-5} m and is estimated individually for each section (the total width or diameter of the section is approximately 0.09 m). Linear interpolation is used between image columns to estimate subpixel resolution L^{obs} decimals.

The inclusion density in the classified image is the fraction of dark pixels. This includes voids, brine pockets, and channels. The inclusion density is estimated for the whole image sample.

4 Results

A total of 69 image samples from the 25 cores, shown in Figure 8, have been processed here. These have been categorized into different sections: 6 lead/new ice, 17 first-year ice, 23 EMIRAD footprint first-year ice, 5 level second-year ice, 13 melt pond, and 5 hummock image samples and into a vertical (V) or a horizontal (H) cut of the core.

4.1 The sea ice salinity

The salinity of the full and partial cores extracted near the cores used for image analysis is shown in Figure 9.

The new ice from the leads was collected during the lead opening events on 23 and 24 January and 5 February 2020. Due to the low air temperatures, the new ice is less than a day old. The new ice was not snow covered, but the patches were covered with frost flowers. A detailed salinity analysis showed that the upper 1-2 centimeters of the core had very high salinities of 35 and 46 ppt, while the salinity at mid depth was 8 to 15 ppt and the bottom layer had salinities of 15 ppt (Figure 10).

https://doi.org/10.5194/egusphere-2026-1440
Preprint. Discussion started: 18 March 2026

First-year ice was sampled at five different sites: 1) Dark Site, young first-year ice approximately 0.72 m thick in a refrozen lead, 2) Biogeochemical 1 mature first-year ice sampling site near the ship, 3) EMIRAD footprint, mature first-year ice about 1.09 - 1.88 m near the ship formed after maneuvering the ship in position, 4) End-of-runway, mature first-year ice, 5) Southern Transect, mature first-year ice. From visual inspection, of the photographs all first-year ice samples fall into the category of "columnar ice".

The refrozen melt pond was a large melted-through melt pond (~ 100 m) surrounded by SYI. The ice salinity profile measured on 11 February 2020 in a 1.26 m core and the ice section photographs indicates that before freezing a freshwater lens of about 0.31 m was capping the saline ocean waters beneath so that the surface ice, measured in 0.03 and 0.05-m sections, was brackish (salinity 0.6 - 2.4 ppt) and the ice beneath was saline (4.6 - 10.9 ppt) (see Figure 9). The surface ~0.22 m of the brackish ice had large air bubbles (centimeter sized) followed by a clear ice layer from ~0.22 to ~0.31 m and then a microstructure of brine pockets below ~0.31 m.

The level second-year ice was sampled near the remote sensing site 2 and the hummock. The thickness measured on 29 January 2020 was between 1.09 and 1.48 m. The salinity of the upper 0.28 m of the ice was 0.7 to 0.9 ppt measured in 6 to 8 sections of the core, and at a deeper depth of 0.28 to 0.43 m the salinity increased to 3.7 and 5.1 ppt (see Figure 9).

The second year ice hummock was sampled near remote sensing site 2 and the melt-pond. The hummock, measured on 29 January 2020, was approximately 2.93 m thick and the upper 0.36 m of the ice had very low salinity of 0.04 ppt to 0.12 ppt per volume and densities, estimated from 0.05 - 0.07 m sections of the core by weight and dimensions, were 535 kg/m^3 at the surface gradually increasing to 808 kg/m^3 at 0.36 m.

4.2 The image analysis

The 2.5, 50 and 97.5 percentiles of the L^{obs} distribution and L^{exp} are shown in Figure 8 for the ordinary image sample (L_x) in blue and the transposed image sample (L_z) in red. When looking at the vertically cut image samples of the columnar new- and first-year ice it is clearly anisotropic with ordinary autocorrelation lengths much shorter than the transposed ones. The anisotropy ratio (L_z/L_x) for new and first-year ice samples is 1.6 to 4.9. For the Dark Site, End-of-runway and Biogeochemical 1 first-year ice samples the anisotropy increases as a function of depth.

A summary of each sample analysis for the full dataset is given in Tables 2, 3, 4, 5 including name, date and core cut direction (V: vertical and H: horizontal), depth from the ice surface [cm], sample salinity or salinity range from above and below the sample for horizontal core cuts, estimated density from sample weight and dimensions [kg/m^3] where this was possible, the density of inclusions in the image (as a fraction of one where 0 is no inclusions and 1 has 100% inclusions), the 50-percentile L_x, the mean L_x, the ordinary L^{exp}, the 50-percentile transposed L^{obs}, the mean transposed L^{obs}, and the transposed L^{exp}. We have also selected two lead / new ice samples in Table 6 to show the typical new ice image samples and the corresponding properties (depth, salinity, density, sample size) and the derived parameters (I_{ID}, L).

The structure of the new ice is anisotropic as seen in Tables 2 with L_z/L_x ratios between 1.7 and 2 for vertically cut cores. The L^{obs} percentiles for the new ice are shown in Figure 11. The average 50 percentile L_x^{obs}, mean L_x^{obs} and L_x^{exp} are 0.17, 0.19 and 0.18 mm, respectively, while the averages of the transposed image samples are 0.29, 0.35, 0.32 mm, respectively.

https://doi.org/10.5194/egusphere-2026-1440
Preprint. Discussion started: 18 March 2026

Compared with vertically cut and horizontally cut image samples in two adjacent 10 cm deep cores (Lead opening event on 24 January 2020, ice thickness 0.10 m), we see that the correlation lengths are comparable for the ordinary direction in the vertically cut image sample; the mean L_x^{obs} is 0.2 mm in the vertical cut and the mean L^{obs} along the predominant direction of the brine pockets of 0.25 mm and across the elongated brine pockets of 0.15 mm in the horizontal cut at a depth of 0.05 m. The vertically cut image sample v2 has a lower mean L_x^{obs} of 0.14 mm. How exactly the vertical cut orients with the L_x/L_y anisotropy is unknown. The three samples were prepared from three separate cores.

For the vertically cut first-year ice samples in Table 3 and the example images in Table 7 and Table 8 are highly anisotropic with the L_z/L_x ratios for the 50 percentile, mean L^{obs} and L^{exp} are between 2.9 and 3.0 and the ordinary autocorrelation lengths are 0.17, 0.19, 0.18 mm. The transposed values are 0.48, 0.56, 0.51 mm. Figure 11 shows the L^{obs} percentiles. When comparing the vertically cut and horizontally cut image samples in two adjacent cores (End-of-runway collected on 16 February 2020) we see that the mean L_x^{obs}s are comparable 0.12 to 0.16 mm in the vertical cut and 0.16 to 0.20 mm in the horizontal cut. A complete matchup is not expected since the horizontal cut is at one specific depth and the vertical cut is over a depth range of ~0.09 m. In addition, the samples were prepared from two separate adjacent cores.

Almost the same values for the vertically cut EMIRAD footprint first-year ice in Table 4 as the first-year ice in Table 3. The L_z/L_x anisotropy ratio is between 2.9-3.1 illustrated in Figure 11. The ordinary autocorrelation lengths; the average 50 percentile L_x^{obs}, mean L_x^{obs} and L_x^{exp} are 0.15, 0.17, 0.16 mm. The transposed ones (L_z) are 0.44, 0.53, and 0.56 mm, respectively. On 9 February 2020 two adjacent cores were drilled to assess the local variations. The vertically cut 0.10 m samples of the 0.30 m long core had image inclusion densities from 0.05 to 0.18 in the v1 core and 0.05 to 0.15 in the v2 core. The mean L_x^{obs}s are also quite similar; 0.11 to 0.18 mm in v1 and 0.14 to 0.20 mm in v2. On 22 February 2020 two adjacent cores were drilled and cut horizontally and vertically to characterize the microstructure in both planes. For the three ordinary image samples to a depth of 30 cm, the mean L_x^{obs} varied for the vertical cut between 0.12 and 0.21 mm and the horizontal cut between 0.16 and 0.30 mm. For all EMIRAD footprint image samples, the surface samples have longer autocorrelation lengths (L_x) than for samples deeper than 0.10 m. Six image samples have been selected in Table 7 and Table 8 to show the typical structure of brine pockets in first-year ice.

The anisotropy in the melt pond, level second-year ice and hummock is much lower than for new- and first-year ice as seen in Table 5. The melt pond with the highest L_z/L_x ratios of 1.4 and 1.7 and the level second-year ice and the hummock being almost isotropic. The diversity in autocorrelation length is high and the average mean L^{obs}s for the 5 level second-year ice samples and two cores at different depths is 0.40 mm (L_x) and 0.46 mm (L_z). The average mean L^{obs} for the melt pond samples at different depths is 0.30 mm (L_x) and 0.43 mm (L_z) with a high diversity of 0.18 to 0.66 mm (L_x) and 0.18 to 0.89 mm (L_z) and the five image samples from two cores in hummocks; 0.45 mm (L_x), 0.49 mm (L_z). Note that the hummocks were sampled at some depth below the surface between 0.20 and 0.40 m (except for one at 0.10 m on 18 January 2020). Surface samples could not be prepared in the laboratory because they had a texture more like snow than ice. Image samples, shown in Table 9, of second-year level ice, melt pond, and hummock were selected to show the distribution of air bubbles and voids in these types of ice.

https://doi.org/10.5194/egusphere-2026-1440
Preprint. Discussion started: 18 March 2026

4.3 The image parameters and salinity

The lead / new ice samples have a high salinity in the range of 8.1 to 18.6 ppt with a mean of 13.1 ppt compared to the first-year ice with a mean of 6.5 ppt. The new ice samples have image inclusion densities of 0.09 to 0.18 and a mean of 0.16 while the first-year ice image samples have a mean of 0.12. On average, there is a relationship between salinity and inclusion density, but we do not have enough data points to properly characterize this relationship shown in Figure 12.

The ordinary mean L_x^{obs} is a function of image inclusion density (I_{ID}) as seen in Figure 13. The best-fit line is $L_x^{obs} = 0.59(I_{ID}) + 0.11$.

The mean L^{obs} is related to L^{exp} for both L_x (Figure 14) and L_z (Figure 15). The blue one-to-one line is shown for reference. There is a tendency for L^{exp} to be larger than L^{obs} for higher L^{obs}, but in general the exponential model makes a good approximation to the estimated autocorrelation function.

5 Discussions

The collection of the surface cores and the processing of the thin sections was an addition to the baseline MOSAiC program, and therefore the collected data set has limitations in terms of temporal (January and February 2020) and spatial extent (selected ice types near the ship), laboratory time, and sites where the cores could be extracted. Despite these limitations, samples from the main types of ice (new ice, FYI, SYI, meltpond, and hummock) in the Arctic Ocean were collected and analyzed. Since there is a limited number of samples, we have presented a summary of each sample analysis in Tables 2, 3, 4, 5.

5.1 The image classification

The success, when the derived parameters do not change as a function of the classification threshold, depends on the image contrast. We have applied adaptive threshold classification with a window size of 0.015 x 0.015 m to all images and a threshold at the window mean minus 30. A change of this threshold to the window mean minus 20 consistently increases the inclusion density by an average of 0.032. However, both the ordinary and transposed autocorrelation lengths are robust to this threshold change, as shown in Figure 16.

For example, changing the threshold to the window mean minus 20 in the Dark Site sample in Figure 3 changes the image inclusion density from 0.14 to 0.18. The ordinary correlation lengths (50-percentile L_x^{obs}, mean L_x^{obs}, and L^{exp}) increase by 0.01 mm each, and the transposed autocorrelation lengths increase by approximately 13%. The Dark Site sample is one of the image samples with the poorest contrast. On average for all samples, the L_x^{obs} increase by 0.0003 mm and L_z^{obs} by 0.02 mm when changing the threshold from 30 to 20. This shows that while the image inclusion density (I_{ID}) is sensitive to the classification threshold, the correlation lengths are relatively robust, with the ordinary L_xs being the most robust.

In the image analysis, we have not distinguished between brine pockets and air bubbles and, in most cases, judging from visual inspection, these two inclusion types do not appear together within the images. Exceptions are image sections in Biogeochemical 1 and the EMIRAD footprint, and here the brine pockets dominate as inclusions. The inclusions of the melt pond change from air bubbles in the upper part of the core (<31 cm) to brine-pockets below. We have flagged (with *) those image samples in which air bubbles and brine pockets appear.

Nghiem et al. (1995b) found that there is a horizontal anisotropy ratio in the correlation lengths of new ice L_y/L_x of 7. We also found a horizontal anisotropy in the new ice. However, the L_y/L_x ratio was much smaller: 1.4.

5.2 Exponential model fit

The exponential model fit to the estimated autocorrelation function is a function of the shifts over which the fit is estimated. Here, we have selected the shift range 0-2L^{obs}. Had the fit been performed in the range 0-L^{obs} then a nearly perfect fit could have been achieved for shifts in that range, but for larger shifts the fit would be poor in most cases. With the 0-2L^{obs} fitting range, the exponential model ACF overestimates the observed ACF for sifts shorter than L^{obs} and underestimates the ACF for shifts longer than L^{obs} in some cases.

As seen in Figures 14 and 15 there is in fact a reasonably good relationship between the 50-percentile L^{obs} and L^{exp} for both ordinary and transposed image samples, which is an indication that the exponential ACF is related to the observed ACF.

When deriving the autocorrelation lengths, it is important that the image lines have a sufficient length, at least $50L_0$. For full image lines of 0.09 m L^{obs} can be estimated with reasonable accuracy up to 1.8 mm. Columnar first-year and second-year ice sometimes have image lines with L^{obs} larger than 1.8 mm, and these have still been estimated with higher uncertainty.

There are strong vertical gradients in the I_{ID} and size in the ice surface layers. These trends will affect the estimation of L^{obs} in the vertical direction and contribute to uncertainty.

5.3 Relation to large-scale modeling

To be able to relate the areal fraction of the brine pocket derived from the image, the correlation lengths, and the inclusion density to large-scale parameters such as salinity (and temperature), we explored the relationship between what is classified as brine in the new and first-year ice image samples and the salinity of the ice shown in Figure 12. This is not trivial, as optical scattering and refraction may not be directly related to the volume of the brine of the sample and the brine pockets can be partially filled with air (Shokr and Sinha (2016)). In addition, the image inclusion density is a function of the classification threshold.

Fortunately, L^{obs} fall within a relatively narrow range for first-year ice [0.11 < mean L_x^{obs} < 0.30] and it is a function of I_{ID} ($L_x^{obs} = 0.59 I_{ID} + 0.11$). The L_z/L_x anisotropy ratio has values near 3. In addition, the mean of the new ice L_x^{obs} falls within a narrow range [0.12 < mean L_x^{obs} < 0.22] and the anisotropy ratio is close to 2. These ranges could be used to constrain the input to microwave emission and scattering models.

These values for L^{obs} are much shorter than the simulated values reported in Nghiem et al. (1995b) by a factor of about 5 to 10. We do not have an explanation for the discrepancy.

We were unable to characterize the relationship L^{obs} with the new- and first-year ice salinity and we were unable to confirm the systematic horizontal anisotropy ratio of 7 as reported by Nghiem et al. (1995b) due to an insufficient number of samples. However, the lead / new-ice sample from 24 January 2020 showed a horizontal anisotropy (L_y/L_x) of 1.4.

6 Conclusions

The brine pocket and air bubble correlation lengths for microwave scattering applications have been derived from a set of thin sections collected and processed during leg 2 (winter leg: December 2019 - February 2020) on the MOSAiC expedition to the Central Arctic Ocean. We found that there is a relationship between the image inclusion density in thin sections and the mean L^{obs}s, which is important to apply the results of this study together with large-scale modeling. We found that the mean L^{obs} for new-ice was 0.12-0.22 mm and first-year 0.11-0.30 mm to be very consistent. The L_z/L_x anisotropy ratio for new and first-year ice is approximately 2-3. Other second-year ice types have a wider range of mean L^{obs} with much smaller anisotropy. The average mean L^{obs} for the second-year-level ice is 0.40 mm (L_x) and 0.46 mm (L_z). The average mean L^{obs}s for the melt pond is 0.30 mm (L_x) and 0.43 mm (L_z) with high diversity and hummocks; 0.45 mm (L_x), 0.49 mm (L_z).

As a final note for future campaigns, we recommend using a larger core diameter for larger samples since short (0.09 m) sample lines compromise the L^{obs} estimation of elongated brine pockets and large air bubbles in sea ice.

Data availability. The complete non-processed image data collection is publicly available following the link:

https://doi.org/10.11583/DTU.31574149

Author contributions. The samples were collected and processed in the lab by RT with the help of VN, JS and MH. The analysis and writing of the manuscript was done by RT with the help of all coauthors.

Competing interests. The authors John Yackel, Vishnu Nandan and Lars Kaleschke are members of “The Cryosphere” editorial board.

Acknowledgements. The authors thank L. N. Friis, N. Z. L. Madsen, T. S. Kristensen, D. S. Holsko, A. B. Christensen, and M. Westermann, V. Isaksen, A. Borre, and K. Berg-Munch for their student projects discussing different aspects of the data. The European Space Agency and the Danish Meteorological Institute are acknowledged for supporting RTT’s participation in MOSAiC.

https://doi.org/10.5194/egusphere-2026-1440
Preprint. Discussion started: 18 March 2026

References

Dierking, W.: Quantitative Roughness Characterisation of Geological Surfaces and Implications for Radar Signature Analysis, IEEE Transactions on Geoscience and Remote Sensing, 37, 1855–1867, 1999.

Lieblappen, R. M., Kumar, D. D., Pauls, S. D., and Obbard, R. W.: A network model for characterizing brine channels in sea ice, The Cryosphere, 12, 1013–1026, https://doi.org/10.5194/tc-12-1013-2018, 2018.

Mätzler, C.: Applications of the Interaction of Microwaves with the Natural Snow Cover, Remote Sensing Reviews, 2, 259–387, https://doi.org/10.1080/02757258709532086, 1987.

Mätzler, C.: Improved Born Approximation for Scattering of Radiation in a Granular Medium, Journal of Applied Physics, 83, 6111–6117, https://doi.org/10.1063/1.367496, 1998.

Nakawo, M. and Sinha, N. K.: Growth Rate and Salinity Profile of First-Year Sea Ice in the High Arctic, Journal of Glaciology, 27, 315–330, https://doi.org/10.3189/S0022143000015409, 1981.

Nakawo, M. and Sinha, N. K.: A note on brine layer spacing of first-year sea ice, Atmosphere - Ocean, 22, 193–206, 1984.

Nghiem, S. V., Kwok, R., Yueh, S. H., and Drinkwater, M. R.: Polarimetric Signatures of Sea Ice, 1. Theoretical Model, Journal of Geophysical Research, 100, 13 665–13 679, 1995a.

Nghiem, S. V., Kwok, R., Yueh, S. H., and Drinkwater, M. R.: Polarimetric Signatures of Sea Ice, 2. Experimental observations, Journal of Geophysical Research, 100, 13 681–13 698, 1995b.

Nicolaus, M., Perovich, D. K., Spreen, G., Granskog, M. A., et al.: Overview of the MOSAiC expedition: Snow and sea ice, Elementa: Science of the Anthropocene, 10, 000 046, https://doi.org/10.1525/elementa.2021.000046, 2022.

Oggier, M. and Eicken, H.: Seasonal evolution of granular and columnar sea ice pore microstructure and pore network connectivity, Journal of Glaciology, 68, 833–848, https://doi.org/10.1017/jog.2022.1, 2022.

O'Sadnick, M., Ingham, M., Eicken, H., and Pettit, E.: In situ field measurements of the temporal evolution of low-frequency sea-ice dielectric properties in relation to temperature, salinity, and microstructure, The Cryosphere, 10, 2923–2940, https://doi.org/10.5194/tc-10-2923-2016, 2016.

Perovich, D. K. and Gow, A. J.: A statistical description of the microstructure of young sea ice, Journal of Geophysical Research: Oceans, 96, 16 943–16 953, https://doi.org/https://doi.org/10.1029/91JC01594, 1991.

Pringle, D. J., Miner, J. E., Eicken, H., and Golden, K. M.: Pore space percolation in sea ice single crystals, Journal of Geophysical Research: Oceans, 114, https://doi.org/https://doi.org/10.1029/2008JC005145, 2009.

Shokr, M. and Sinha, N.: Sea Ice: Physics and Remote Sensing, vol. 209 of *Geophysical Monograph Series*, American Geophysical Union and Wiley, 2016.

Shokr, M. and Sinha, N. K.: Ice Physics and Physical Processes, chap. 2, pp. 29–105, John Wiley Sons, Ltd, https://doi.org/https://doi.org/10.1002/9781119828242.ch2, 2023.

Shokr, M. E.: Field observations and model calculations of dielectric properties of Arctic sea ice in the microwave C-band, IEEE Transactions on Geoscience and Remote Sensing, 36, 463–478, https://doi.org/10.1109/36.662730, 1998a.

Shokr, M. E.: Field observations and model calculations of dielectric properties of Arctic sea ice in the microwave C-band, IEEE Transactions on Geoscience and Remote Sensing, 36, 463–478, https://doi.org/10.1109/36.662730, 1998b.

Tonboe, R., Andersen, S., Toudal, L., and Heygster, G.: Sea Ice Emission Modelling Applications, in: Thermal Microwave Radiation: Applications for Remote Sensing, edited by Mätzler, C. et al., vol. 52 of *IET Electromagnetic Waves Series*, pp. 382–400, IET, London, U.K., 2006.

Tonboe, R. T.: Modeling Microwave Emission and Scattering from Snow-Covered Sea Ice, Wiley, 2 edn., https://doi.org/10.1002/9781119828242.ch12, 2023.

Tonboe, R. T., Nandan, V., Makynen, M. P., Pedersen, L. T., Kern, S., Lavergne, T., Oelund, J., Dybkjar, G., Saldo, R., and Huntemann, M.: Simulated Geophysical Noise in Sea Ice Concentration Estimates of Open Water and Snow-covered Sea Ice, IEEE Journal of Selected Topics in Applied Earth Observations and Remote Sensing, 15, 1309–1326, https://doi.org/10.1109/JSTARS.2021.3134021, 2022.

Tsang, L. and Ishimaru, A.: Radiative Wave Equations for Vector Electromagnetic Propagation in Dense Non-Tenuous Media, Journal of Electromagnetic Waves and Applications, 1, 59–72, 1987.

Ulaby, F. T. and Long, D. G.: Microwave Radar and Radiometric Remote Sensing, University of Michigan Press, 2014.

Vallese, F. and Kong, J. A.: Correlation Function Studies for Snow and Ice, Journal of Applied Physics, 52, 4921–4925, 1981.

Weeks, W. F. and Ackley, S. F.: The Growth, Structure and Properties of Sea Ice, in: The Geophysics of Sea Ice, edited by Untersteiner, N., vol. 146 of *NATO ASI Series, Series B: Physics*, Springer, 1986.

Wiesmann, A., Mätzler, C., and Weise, T.: Radiometric and Structural Measurements of Snow Samples, Radio Science, 33, 273–289, 1998.

https://doi.org/10.5194/egusphere-2026-1440
Preprint. Discussion started: 18 March 2026

Tables

Table 1 List of processed core sample extraction dates, locations (see Figure 1) and orientation of cut direction.

Jan. 16. 2020	Level SYI (Remote sensing site - 2), vertical
Jan. 18. 2020	Hummock (Remote sensing site - 2), horizontal
Jan. 19. 2020	First-year ice (EMIRAD footprint), vertical
Jan. 22. 2020	Refrozen melt-pond (Remote sensing site - 2), vertical
Jan. 22. 2020	Refrozen melt-pond (Remote sensing site - 2), vertical
Jan. 23. 2020	Lead new ice (Southern transect), vertical
Jan. 24. 2020	Lead new ice (Southern transect), 2 x vertical, horizontal
Jan. 24. 2020	First-year ice (Southern transect), vertical, horizontal
Jan. 29. 2020	Refrozen melt-pond (Remote sensing site - 2), horizontal
Feb. 2. 2020	Refrozen melt-pond (Remote sensing site - 2), horizontal
Feb. 2. 2020	Level SYI (Remote sensing site - 2), horizontal
Feb. 5. 2020	First-year ice (Dark site), vertical
Feb. 5. 2020	Lead young ice (Dark site), vertical
Feb. 9. 2020	First-year ice (EMIRAD footprint), vertical, 2 x horizontal
Feb. 11. 2020	Refrozen melt-pond (Remote sensing site - 2), vertical
Feb. 12. 2020	Level SYI (Remote sensing site - 2), vertical
Feb. 12. 2020	Hummock (Remote sensing site - 2), vertical
Feb. 16. 2020	First-year ice (EMIRAD footprint), vertical
Feb. 16. 2020	First-year ice (End-of-runway), vertical, horizontal
Feb. 20. 2020	First-year ice (Biogeochemical 1), vertical
Feb. 22. 2020	First-year ice (EMIRAD footprint), horizontal

Table 2 New ice samples from lead opening events. A: Name, date (YYYYMMDD) and cut direction (vertical: V and horizontal: H), B: depth of sample [cm], C: sample salinity or salinity range from above and below the sample for horizontal cuts, D: estimated density from sample weight and dimensions [kg/m^3] where this was possible, E: the density of inclusions in the image [fraction of one], F: the 50-percentile ordinary L_x^{obs}, G: the mean ordinary L_x^{obs}, H: the ordinary L_x^{exp}, I: the 50 percentile transposed L_z^{obs}, J: the mean transposed L_z^{obs}, K: and the transposed L_z^{exp}.

A	B	C	D	E	F	G	H	I	J	K
Lead 20200123 V	0-7.5	17.0	-	0.18	0.19	0.21	0.20	0.31	0.36	0.33
Lead v1 20200124 V	0-10	10.5	-	0.16	0.18	0.20	0.19	0.36	0.46	0.42
Lead v2 20200124 V	0-10	11.2	-	0.11	0.12	0.14	0.13	0.30	0.37	0.32
Lead 20200124 H	5	8.1-8.6	-	0.18	0.22	0.24	0.23	0.16	0.17	0.17
Lead 20200205 V	0-7.5	18.6	-	0.18	0.20	0.22	0.21	0.19	0.20	0.20
Lead 20200205 V	7.5-15	10.9	-	0.09	0.16	0.16	0.16	0.24	0.28	0.25

Table 3 Various first-year ice samples. A: Name, date (YYYYMMDD) and cut direction (vertical: V and horizontal: H), B: depth of sample [cm], C: sample salinity or salinity range from above and below the sample for horizontal cuts, D: estimated density from sample weight and dimensions [kg/m^3] where this was possible, E: the density of inclusions in the image [fraction of one], F: the 50 percentile ordinary L_x^{obs}, G: the mean ordinary L_x^{obs}, H: the ordinary L_x^{exp}, I: the 50 percentile transposed L_z^{obs}, J: the mean transposed L_z^{obs}, K: and the transposed L_z^{exp}. (*)Air bubbles and brine pockets in the sample.

A	B	C	D	E	F	G	H	I	J	K
Southern transect* 20200124 V	0-10	5.7	-	0.15	0.19	0.20	0.20	0.28	0.32	0.30
Southern transect 20200124 H	20	4.2-5.9	907-919	0.11	0.16	0.17	0.16	0.17	0.17	0.17
Southern transect 20200124 H	30	5.9	919-919	0.14	0.24	0.27	0.25	0.23	0.26	0.25
Southern transect 20200124 H	40	4.3	919-924	0.09	0.16	0.17	0.16	0.17	0.17	0.17
Dark site 20200205 V	0-10	15.2	-	0.13	0.16	0.18	0.17	0.36	0.48	0.41
Dark site 20200205 V	10-20	8.5	-	0.14	0.21	0.24	0.23	0.66	0.76	0.71
Dark site 20200205 V	20-30	7.2	-	0.11	0.15	0.16	0.15	0.46	0.58	0.49
End-of-runway* 20200216 V	0-9	-	-	0.10	0.16	0.19	0.16	0.46	0.53	0.47
End-of-runway 20200216 V	9-18	-	-	0.07	0.13	0.14	0.13	0.46	0.56	0.48
End-of-runway 20200216 V	18-27	-	-	0.09	0.12	0.12	0.12	0.52	0.60	0.52
End-of-runway 20200216 H	2	-	913	0.16	0.20	0.21	0.20	0.19	0.20	0.20
End-of-runway 20200216 H	12	-	906-913	0.10	0.16	0.18	0.16	0.19	0.23	0.19
End-of-runway 20200216 H	22	-	906	0.08	0.19	0.20	0.18	0.17	0.18	0.17
Biogeochemical 1* 20200220 V	0-10	4.7	-	0.21	0.19	0.23	0.21	0.42	0.48	0.44
Biogeochemical 1* 20200220 V	10-20	4.7	931	0.16	0.18	0.22	0.20	0.46	0.51	0.48
Biogeochemical 1 20200220 V	20-30	4.4	950	0.11	0.18	0.20	0.19	0.71	0.81	0.75
Biogeochemical 1 20200220 V	30-40	4.3	947	0.08	0.15	0.15	0.15	0.67	0.73	0.64

Table 4 All EMIRAD footprint first-year ice samples. A: Name, date (YYYYMMDD) and cut direction (vertical: V | horizontal: H), B: depth of sample [cm], C: sample salinity or salinity range from above and below the sample for horizontal cuts, D: estimated density from sample weight and dimensions $[kg/m^3]$ where this was possible, E: the density of inclusions in the image [fraction of one], F: the 50 percentile ordinary L_x^{obs}, G: the mean ordinary L_x^{obs}, H: the ordinary L_x^{exp}, I: the 50 percentile transposed L_z^{obs}, J: the mean transposed L_z^{obs}, K: and the transposed L_z^{exp}. (*)Air bubbles and brine pockets in the sample.

A	B	C	D	E	F	G	H	I	J	K
EMIRAD footprint* 20200119 V	0-13	14.2	-	0.18	0.24	0.27	0.26	0.41	0.48	0.44
EMIRAD footprint 20200119 V	13-22	7.4	-	0.09	0.14	0.15	0.14	0.57	0.67	0.57
EMIRAD footprint 20200119 V	22-31	5.4	-	0.08	0.12	0.12	0.12	0.41	0.50	0.41
EMIRAD footprint v1* 20200209 V	0-10	10.4	-	0.18	0.16	0.18	0.17	0.32	0.38	0.35
EMIRAD footprint v1 20200209 V	10-20	3.8	-	0.05	0.11	0.11	0.10	0.35	0.45	0.37
EMIRAD footprint v1 20200209 V	20-30	4.2	-	0.06	0.11	0.12	0.12	0.45	0.57	0.47
EMIRAD footprint v2 20200209 V	0-10	-	-	0.15	0.17	0.18	0.17	0.46	0.55	0.49
EMIRAD footprint v2 20200209 V	10-20	-	-	0.05	0.13	0.14	0.13	0.50	0.63	0.52
EMIRAD footprint v2 20200209 V	20-30	-	-	0.10	0.18	0.20	0.19	0.59	0.69	0.61
EMIRAD footprint* 20200209 H	2	9.3	961	0.30	0.21	0.22	0.22	0.22	0.22	0.22
EMIRAD footprint 20200209 H	10	4.1-9.3	922-961	0.13	0.17	0.17	0.17	0.18	0.19	0.18
EMIRAD footprint 20200209 H	20	4.1-5.7	922-965	0.07	0.11	0.12	0.11	0.15	0.16	0.15
EMIRAD footprint* 20200216 V	0-10	7.9	-	0.15	0.17	0.19	0.18	0.31	0.35	0.33
EMIRAD footprint 20200216 V	10-20	4.5	917	0.09	0.16	0.19	0.17	0.37	0.47	0.41
EMIRAD footprint* 20200216 V	20-30	4.7	934	0.10	0.16	0.16	0.15	0.44	0.50	0.45
EMIRAD footprint* 20200222 V	0-10	5.6	-	0.13	0.17	0.21	0.19	0.42	0.49	0.43
EMIRAD footprint 20200222 V	10-20	4.9	-	0.07	0.13	0.13	0.13	0.55	0.63	0.54
EMIRAD footprint 20200222 V	20-30	5.4	-	0.06	0.12	0.12	0.12	0.41	0.54	0.41
EMIRAD footprint* 20200222 H	2	5.4-7.0	-	0.13	0.25	0.30	0.27	0.24	0.28	0.25
EMIRAD footprint 20200222 H	12	5.0-5.4	-	0.09	0.18	0.19	0.18	0.15	0.16	0.15
EMIRAD footprint 20200222 H	22	4.6-5.0	-	0.12	0.16	0.16	0.15	0.20	0.20	0.19
EMIRAD footprint 20200222 H	32	4.6	-	0.09	0.18	0.18	0.17	0.18	0.18	0.17

Table 5 Level SYI, melt pond and hummocks. A: Name, date (YYYYMMDD) and cut direction (vertical: V | horizontal: H), B: depth of sample [cm], C: sample salinity or salinity range from above and below the sample for horizontal cuts, D: estimated density from sample weight and dimensions $[kg/m^3]$ where this was possible, E: the density of inclusions in the image [fraction of one], F: the 50 percentile ordinary L_x^{obs}, G: the mean ordinary L_x^{obs}, H: the ordinary L_x^{exp}, I: the 50 percentile transposed L_z^{obs}, J: the mean transposed L_z^{obs}, K: and the transposed L_z^{exp}. (*)Air bubbles and brine pockets in the sample.

A	B	C	D	E	F	G	H	I	J	K
Level second year ice 20200116 V	0-7.5	-	-	0.12	0.25	0.47	0.34	0.54	0.67	0.59
Level second year ice 20200116 V	7.5-14	-	-	0.03	0.14	0.19	0.14	0.22	0.29	0.22
Level second year ice 20200129 V	0-10	0.7	900	0.12	0.33	0.36	0.33	0.43	0.48	0.43
Level second year ice 20200212 V	0-10	-	-	0.10	0.25	0.32	0.28	0.34	0.41	0.36
Level second year ice 20200212 V	10-20	-	-	0.09	0.19	0.21	0.20	0.30	0.34	0.31
Level second year ice 20200212 V	20-30	-	-	0.09	0.28	0.52	0.38	0.90	0.95	0.88
Meltpond Ku-Ka 20200122 V	0-8.5	0.8	-	0.25	0.35	0.50	0.47	0.53	0.60	0.56
Meltpond Ku-Ka 20200122 V	8.5-18	0.8	-	0.15	0.30	0.48	0.40	0.70	0.80	0.77
Meltpond SSMI 20200129 H	3	2.1	906	0.21	0.25	0.33	0.27	0.25	0.31	0.27
Meltpond SSMI 20200129 H	10	2.1-4.7	895-906	0.13	0.18	0.19	0.18	0.17	0.18	0.18
Meltpond SSMI 20200129 H	20	2.5-4.7	895-909	0.11	0.49	0.64	0.52	0.52	0.58	0.50
Meltpond SSMI 20200129 H	30	4.8	906	0.15	0.17	0.18	0.17	0.22	0.23	0.22
Meltpond L-SCAT 20200202 H	3	1.3	886	0.07	0.25	0.29	0.26	0.25	0.29	0.26
Meltpond L-SCAT 20200202 H	10	0.9-1.3	886-923	0.05	0.25	0.28	0.26	0.25	0.30	0.26
Meltpond L-SCAT 20200202 H	20	0.9-3.5	923-924	0.07	0.25	0.44	0.32	0.26	0.47	0.34
Meltpond L-SCAT 20200202 H	30	1.2-3.5	918-924	0.08	0.26	0.35	0.28	0.26	0.33	0.28
Meltpond 20200211 V	0-10	1.0	-	0.18	0.56	0.66	0.61	0.72	0.78	0.71
Meltpond 20200211 V	10-20	0.8	-	0.16	0.23	0.46	0.31	0.51	0.62	0.56
Meltpond* 20200211 V	20-30	1.7	-	0.07	0.19	0.35	0.25	0.79	0.89	0.78
Hummock 20200118 H	10	0.1	535-715	0.45	0.22	0.23	0.23	0.22	0.23	0.23
Hummock 20200118 H	20	0.1	715-856	0.37	0.36	0.41	0.39	0.36	0.39	0.39
Hummock 20200118 H	30	0.1	808-856	0.21	0.73	0.79	0.74	0.74	0.76	0.71
Second year ice hummock 20200212 V	20-30	0.1	779	0.31	0.31	0.36	0.34	0.53	0.57	0.53
Second year ice hummock 20200212 V	30-37	0.1	797	0.30	0.39	0.44	0.42	0.54	0.58	0.55

https://doi.org/10.5194/egusphere-2026-1440
Preprint. Discussion started: 18 March 2026

Table 6 Selected examples of lead ice samples. AA: Sample name, date and cut direction, BB: depth of sample [cm], CC: Salinity [ppt], DD: Density [kg/m^3], EE: Image inclusion density [0-1], FF: 2.5, 50, and 97.5-pecentiles of L_x^{obs} in ordinary direction [mm], GG: ordinary mean L_x^{obs} [mm], HH: L_x^{exp} in ordinary direction [mm], II: 2.5, 50, and 97.5 pecentiles of L_z^{obs} in transposed direction [mm], JJ: transposed mean L_z^{obs} [mm], KK: L_z^{exp} in transposed direction [mm], LL: comment, MM: image sample, 1) the sample is new-ice

AA	BB	CC	DD	EE	FF	GG	HH	II	JJ	KK	LL	MM
Lead 20200124 v1 Vertical	0-10	10.5	-	0.16	0.14 0.18 0.36	0.20	0.19	0.19 0.36 1.30	0.46	0.42	90	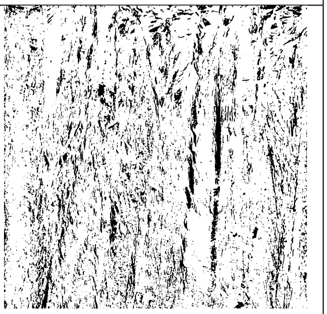
Lead 20200124 Horizontal	5	8.1-8.6	-	0.18	0.14 0.22 0.52	0.24	0.23	0.12 0.16 0.26	0.17	0.17	56	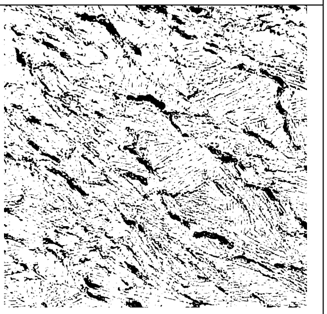

Table 7 First-year ice from End-of-runway, the Dark site, and EMIRAD footprint. AA: Sample name, date (YYYYMMDD) and cut direction, BB: depth of sample [cm], CC: Salinity [ppt], DD: Density [kg/m^3], EE: Image inclusion density [0-1], FF: 2.5, 50, and 97.5 pecentiles of L_x^{obs} in ordinary direction [mm], GG: ordinary mean L_x^{obs} [mm], HH: L_x^{exp} in ordinary direction [mm], II: 2.5, 50, and 97.5-pecentiles of L_z^{obs} in transposed direction [mm], JJ: transposed mean L_z^{obs} [mm], KK: L_z^{exp} in transposed direction [mm], LL: comment, MM: image sample, 1) the sample is columnar first-year ice.

AA	BB	CC	DD	EE	FF	GG	HH	II	JJ	KK	LL	MM
End-of-runway 20200216 Vertical	0-9	-	-	0.10	0.10 0.16 0.61	0.19	0.16	0.19 0.46 1.34	0.53	0.47	76	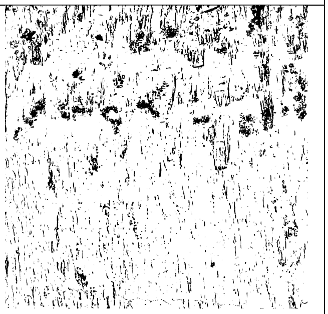
Dark site 20200205 Vertical	10-20	8.5	-	0.14	0.15 0.21 0.63	0.24	0.23	0.20 0.66 1.89	0.76	0.71	84	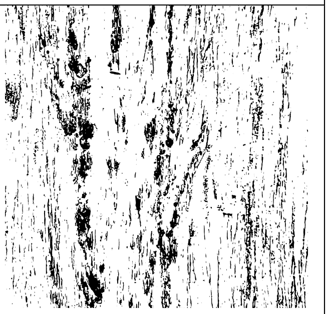
EMIRAD footprint 20200222 Vertical	10-20	4.9	-	0.07	0.10 0.13 0.17	0.13	0.13	0.16 0.55 1.71	0.63	0.54	90	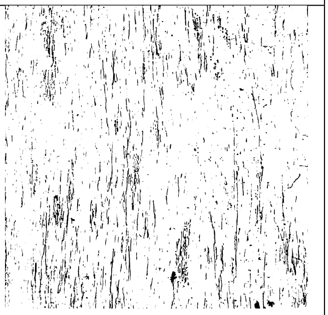

Table 8 First-year ice from Biogeochemical, End-of-runway and Southern transect. AA: Sample name, date (YYYYMMDD) and cut direction, BB: depth of sample [cm], CC: Salinity [ppt], DD: Density $[kg/m^3]$, EE: Image inclusion density [0-1], FF: 2.5, 50, and 97.5 pecentiles of L_x^{obs} in ordinary direction [mm], GG: ordinary mean L_x^{obs} [mm], HH: L_x^{exp} in ordinary direction [mm], II: 2.5, 50, and 97.5-pecentiles of L_z^{obs} in transposed direction [mm], JJ: transposed mean L_z^{obs} [mm], KK: L_z^{exp} in transposed direction [mm], LL: comment, MM: image sample, 1) the sample is columnar first-year ice.

AA	BB	CC	DD	EE	FF	GG	HH	II	JJ	KK	LL	MM
Biogeochemical 1 20200220 Vertical	20-30	4.4	950	0.11	0.13 0.18 0.39	0.20	0.19	0.20 0.71 1.90	0.81	0.75	87	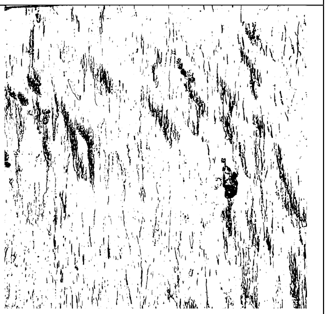
End-of-runway 20200216 Horizontal	2	-	913	0.16	0.15 0.20 0.28	0.21	0.20	0.15 0.19 0.29	0.20	0.20	62	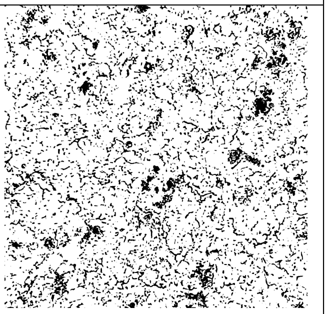
Southern transect 20200124 Horizontal	30	5.9	919-919	0.14	0.15 0.24 0.63	0.27	0.25	0.16 0.23 0.63	0.26	0.25	59	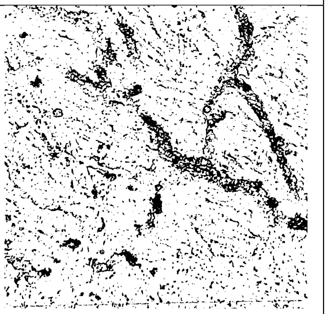

https://doi.org/10.5194/egusphere-2026-1440
Preprint. Discussion started: 18 March 2026

Table 9 Examples of level second year ice, hummock and refrozen meltpond. AA: Sample name, date (YYYYMMDD) and cut direction, BB: depth of sample [cm], CC: Salinity [ppt], DD: Density $[kg/m^3]$, EE: Image inclusion density [0-1], FF: 2.5, 50, and 97.5 pecentiles of L_x^{obs} in ordinary direction [mm], GG: ordinary mean L_x^{obs} [mm], HH: L_x^{exp} in ordinary direction [mm], II: 2.5, 50, and 97.5-pecentiles of L_z^{obs} in transposed direction [mm], JJ: transposed mean L_z^{obs} [mm], KK: L_z^{exp} in transposed direction [mm], LL: comment, MM: image sample

AA	BB	CC	DD	EE	FF	GG	HH	II	JJ	KK	LL	MM
Level second year ice 20200212 Vertical	20-30	-	-	0.09	0.13 0.28 2.03	0.52	0.38	0.22 0.90 2.01	0.95	0.88	90.09	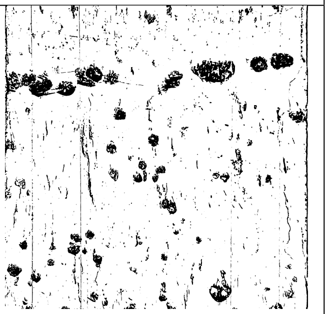
Meltpond 20200211 Vertical	0-10	1.0	-	0.18	0.17 0.56 1.85	0.66	0.61	0.26 0.72 1.66	0.78	0.71	80.03	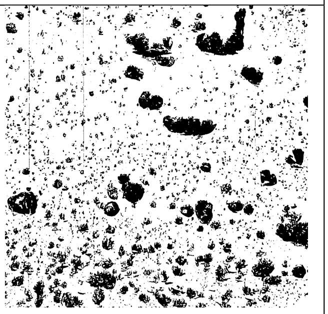
Hummock 20200118 Horizontal	30	0.1	808-856	0.21	0.45 0.73 1.31	0.79	0.74	0.42 0.74 1.22	0.76	0.71	55.62	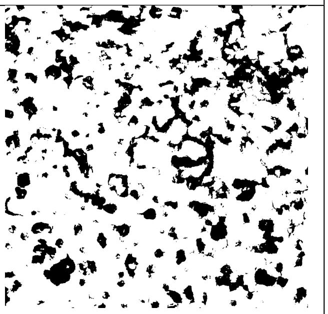

Figures

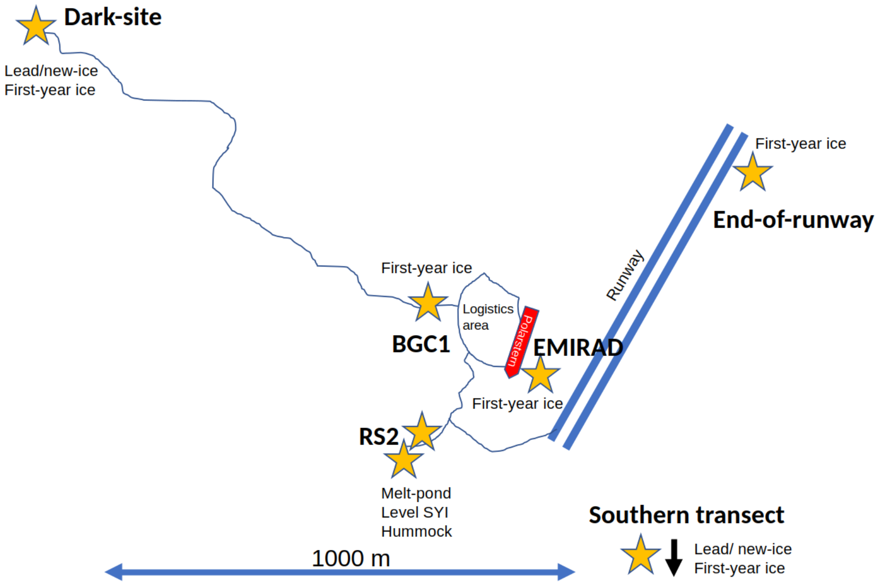

Figure 1. A map illustrating (stars) the sampling locations around R/V Polarstern with typical sea ice types. BGC1 is Biogeochemical 1 and RS2 is Remote Sensing site 2.

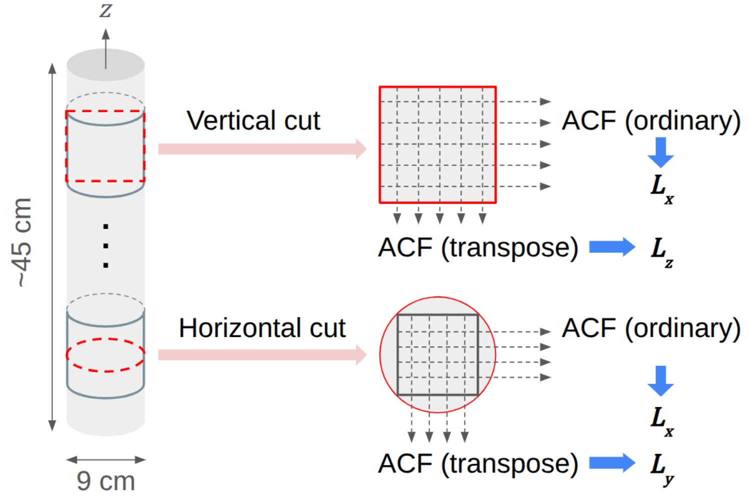

Figure 2. A schematic diagram summarizing the thin section procedures and imaging processing steps to estimate autocorrelation function, ACF, and associated correlation length, L, in three principle directions x, y, z.

https://doi.org/10.5194/egusphere-2026-1440
Preprint. Discussion started: 18 March 2026

Figure 3. An example of a first-year ice sample photograph from Dark Site at about 0.11-0.19 m depth, sampled on Feb. 5., 2020. The sample width and height is 0.084 m. The salinity of the sample is 8.5 ppt

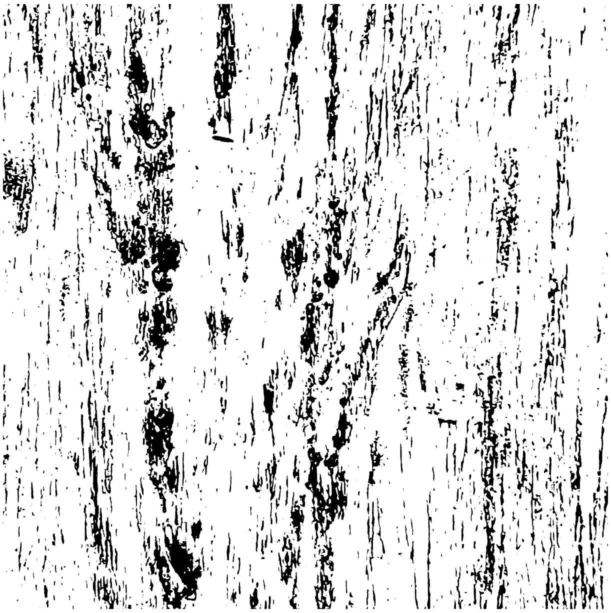

Figure 4. An adaptive threshold classification of the photograph in Figure 3. The threshold is the image mean brightness minus 30.

https://doi.org/10.5194/egusphere-2026-1440
Preprint. Discussion started: 18 March 2026

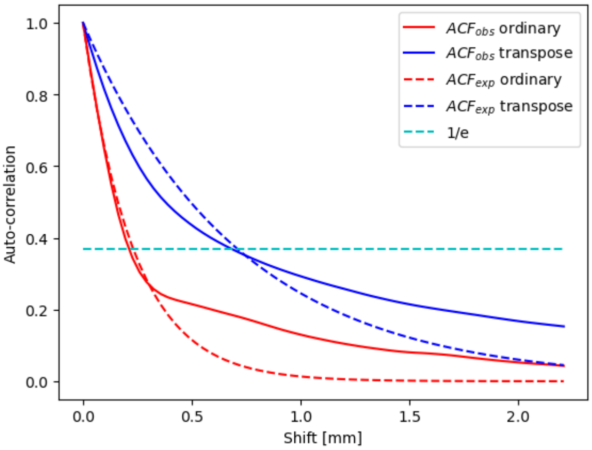

Figure 5. Least-squares fit of the exponential model to the estimated ACF in Figure 4 over the range 0-2L^{obs}. The dashed cyan line is $1/e$.

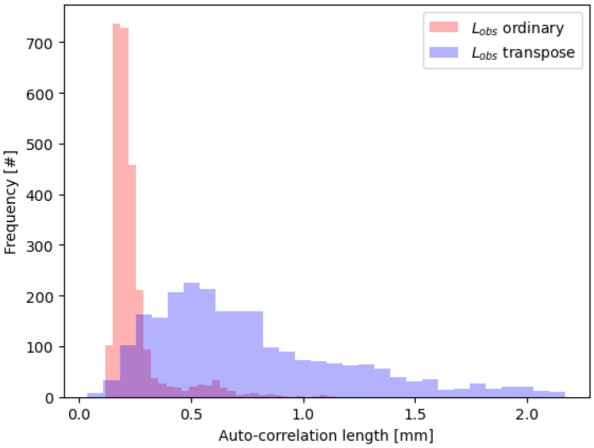

Figure 6. Line by line histogram of estimated auto-correlation lengths (L^{obs}) in Figure 4, ordinary L_x^{obs} (red) and transposed L_z^{obs} (blue).

https://doi.org/10.5194/egusphere-2026-1440
Preprint. Discussion started: 18 March 2026

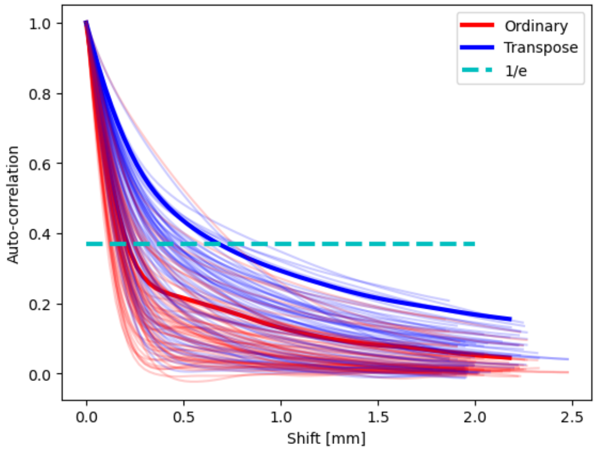

Figure 7. All auto-correlation functions from the 69 image samples, both ordinary (red) and transposed (blue). The Dark Site example from Figure 5 is shown in bold.

https://doi.org/10.5194/egusphere-2026-1440
Preprint. Discussion started: 18 March 2026

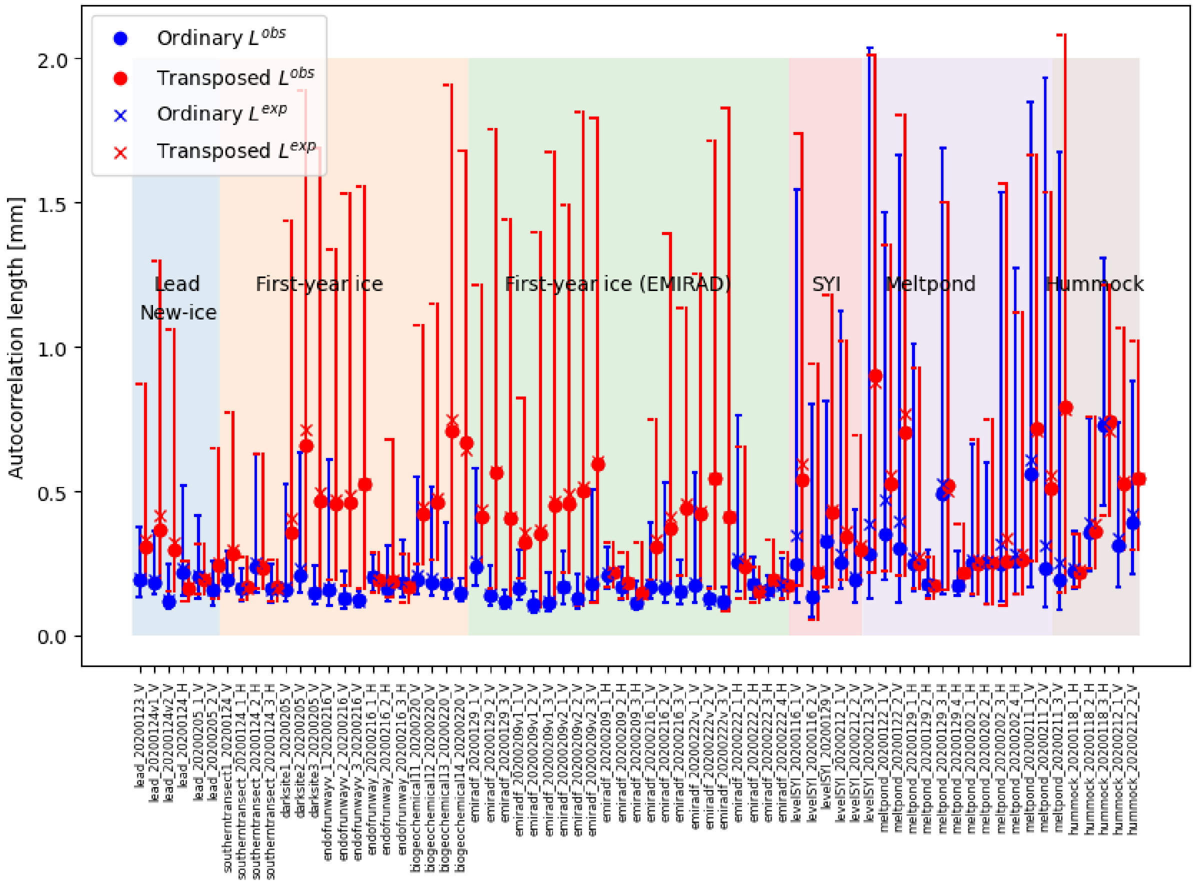

Figure 8. Summary of the correlation length of analyzed samples.

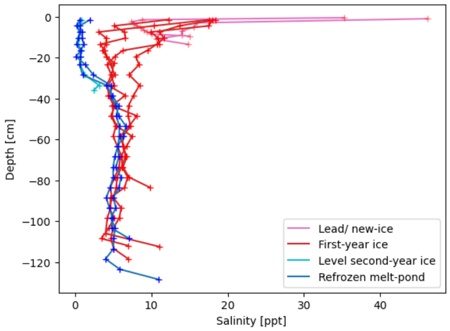

Figure 9. The salinity of lead/ new-ice (Dark Site Feb. 5., 2020 and Southern Transect Jan. 24., 2020), First-year ice (Dark Site Feb. 5., 2020, EMIRAD foot-print Jan. 19., 2020, 2 x Jan. 24., 2020), partial (0.41 m) level second year ice from Remote Sensing Site 2 (Jan. 29., 2020), refrozen melt pond (Remote Sensing Site 2 Jan. 04., 2020 and Feb. 11., 2020). Note that the vertical resolution varies in the cores: Lead/ new-ice 0.01 or 0.02 m resolution, other cores 0.03 m resolution in the top 0.21 m and then 0.05 m resolution.

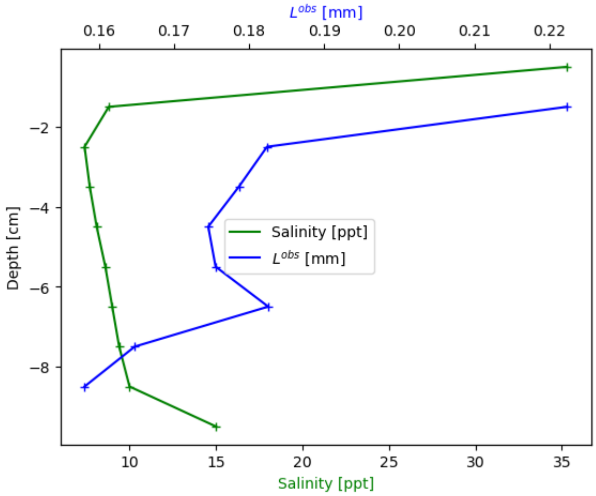

Figure 10. The salinity and the L_x^{obs} for the Southern Transect lead opening event 24 January 2020. Note that L_x^{obs} could not be estimated for the top (0-1 cm) and bottom (9-10 cm) slice.

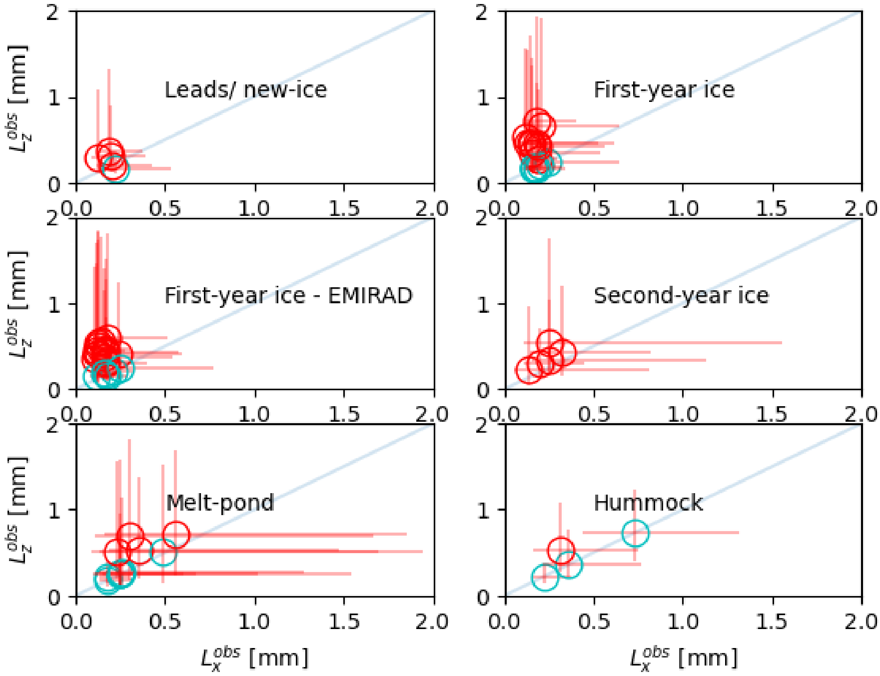

Figure 11. Overview of the L^{obs} confidence intervals [2.5,50,97.5] percentiles for ordinary (L_x) and transposed (L_z). Horizontally cut cores are marked with blue circles and then the ordinary represent L_x and transposed represent L_y.

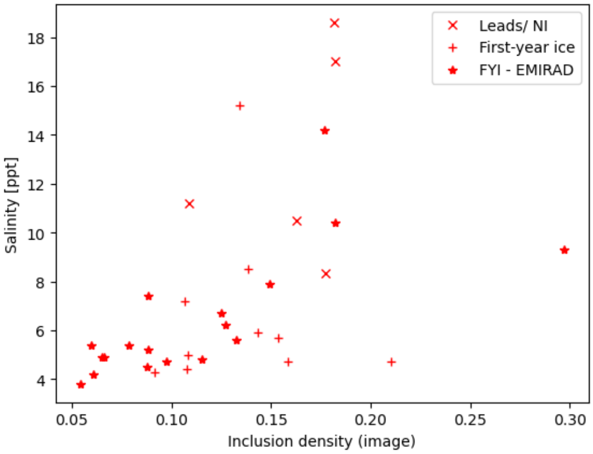

Figure 12. Image inclusion density vs new- and first-year ice salinity.

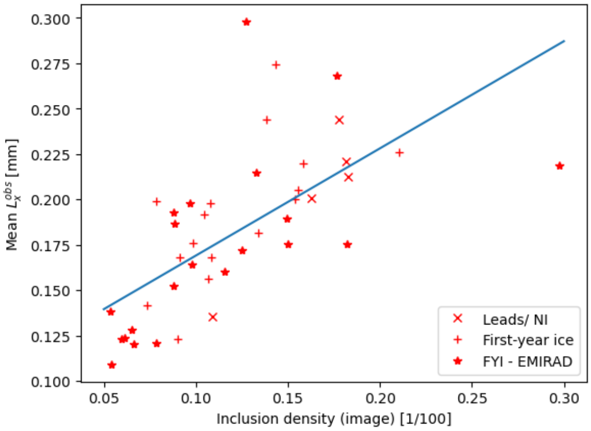

Figure 13. The new and first year ice image inclusion density (I_{ID}) vs mean L_x^{obs}. The blue line is the best-fit to the data points.

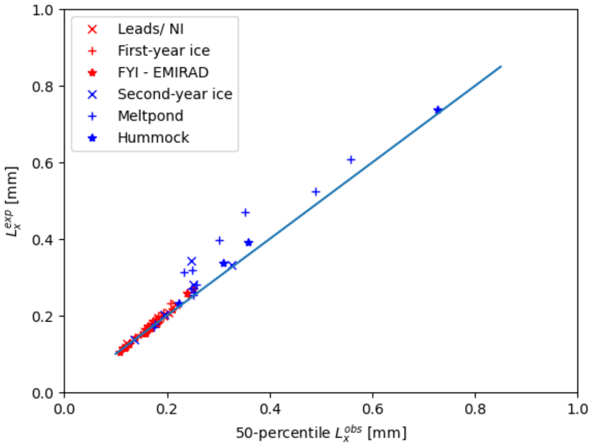

Figure 14. The horizontal 50-percentile L_x^{obs} vs the L_x^{exp} for all sampled ice types.

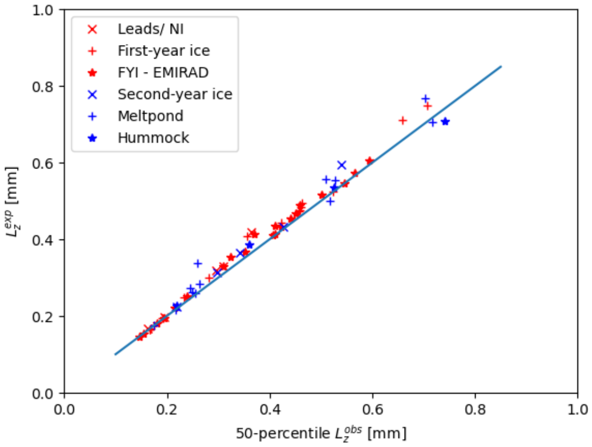

Figure 15. The vertical 50-percentile L_z^{obs} vs the L_z^{exp} for all sampled ice types.

https://doi.org/10.5194/egusphere-2026-1440
Preprint. Discussion started: 18 March 2026

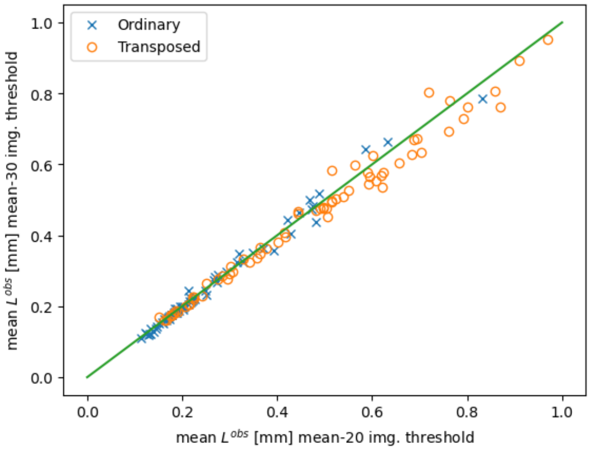

Figure 16. Shows the effect of the image classification threshold (the local mean minus 20 or 30) on the mean L^{obs}.